RESEARCH ARTICLE SUMMARY

ASTEROIDS

Variations in color and reflectance on the surface of asteroid (101955) Bennu

D. N. DellaGiustina*, K. N. Burke, K. J. Walsh, P. H. Smith, D. R. Golish, E. B. Bierhaus, R.-L. Ballouz, T. L. Becker, H. Campins, E. Tatsumi, K. Yumoto, S. Sugita, J. D. Prasanna Deshapriya, E. A. Cloutis, B. E. Clark, A. R. Hendrix, A. Sen, M. M. Al Asad, M. G. Daly, D. M. Applin, C. Avdellidou, M. A. Barucci, K. J. Becker, C. A. Bennett, W. F. Bottke, J. I. Brodbeck, H. C. Connolly Jr., M. Delbo, J. de Leon, C. Y. Drouet d'Aubigny, K. L. Edmundson, S. Fornasier, V. E. Hamilton, P. H. Hasselmann, C. W. Hergenrother, E. S. Howell, E. R. Jawin, H. H. Kaplan, L. Le Corre, L. F. Lim, J. Y. Li, P. Michel, J. L. Molaro, M. C. Nolan, J. Nolau, M. Pajola, A. Parkinson, M. Popescu, N. A. Porter, B. Rizk, J. L. Rizos, A. J. Ryan, B. Rozitis, N. K. Shultz, A. A. Simon, D. Trang, R. B. Van Auken, C. W. V. Wolner, D. S. Lauretta

INTRODUCTION: The color and reflectance of asteroids can be used to infer their compositions and histories. Variations in these spectrophotometric properties are driven by differences in lithology and/or exposure to processes collectively known as space weathering (bombardment by meteoroids and solar wind ions). On anhydrous bodies, such as the Moon and S-type asteroids, space weathering darkens and reddens spectral slopes (where "redder" indicates a more positive slope relative to the solar spectrum) in the visible wavelengths. However, on primitive C-complex asteroids—bodies that may have delivered water and organics to early Earth—the spectral changes that result from space weathering are not well understood. Evidence from meteorites thought to be analogous to C-complex asteroids suggests that either reddening or bluing is possible. Deciphering such changes is necessary to understand the origin and relative exposure age of surface units on primitive Solar System objects.

False-color image mosaic of rubble on asteroid Bennu, as observed with the MapCam multispectral imager. Color and reflectance vary between and within boulders, resulting from different exposure ages and innate compositions. Red is the x/v band ratio (indicating redder spectral slopes), green represents relative change in the w band (an indication of composition), and blue is the b'/v band ratio (indicating bluer spectral slopes in the near-ultraviolet region).

RATIONALE: The MapCam imager on the OSIRIS-REx (Origins, Spectral Interpretation, Resource Identification, and Security–Regolith Explorer) spacecraft acquired global multispectral images of the C-complex asteroid (101955) Bennu in four bands: b' (0.44 to 0.50 μm), v (0.52 to 0.58 μm), w (0.67 to 0.73 μm), and x (0.82 to 0.89 μm). Bennu is a rubble pile, made up of the reaccumulated fragments of a larger C-complex progenitor that was blown apart by a catastrophic impact.

Using band ratios and principal components analysis, we mapped Bennu's color and reflectance at a pixel scale of ~25 cm. In combination with higher-resolution (~5 cm per pixel) panchromatic PolyCam images, we assessed relationships between MapCam spectra and morphologic features on Bennu's surface, aiming to understand sources of variation from the average and determine the relative timing associated with color differences.

RESULTS: The surface of Bennu has unexpectedly heterogeneous colors distributed on a moderately blue (gently negatively sloped) global surface. Boulders are the dominant source of heterogeneity and fall into distinct populations on the basis of reflectance. Dark boulders (reflectance of 0.034 to 0.049, encompassing Bennu's average reflectance of 0.044) tend to be rougher and rounder, whereas bright boulders (0.049 to 0.074) are smoother and more angular. Variation in color within individual boulders is also apparent; for example, boulder faces that appear to be more recently exposed owing to fracturing are bluer than putatively older faces. Conversely, small reddish craters are observed to overlie blue craters, indicating that the former are younger (more recently exposed material). Bennu's smallest craters have a size distribution that indicates that they are also the youngest, and they are redder than the average surface. Many of the larger (older) craters have colors indistinguishable from Bennu's average. Crater spectral slopes indicate that terrains with intermediate ages have the bluest near-ultraviolet spectral slopes.

CONCLUSION: The differences in reflectance and texture among boulders indicate that Bennu may have inherited distinct lithologies formed at different depths in its larger progenitor asteroid, as well as debris from impactors. The color variations within boulders and among craters suggest that space weathering on Bennu does not drive a unidirectional progression from red to blue (or vice versa). Rather, freshly exposed redder surfaces, as exemplified by the small reddish craters, initially brighten in the near-ultraviolet region (i.e., become blue at shorter wavelengths), as exemplified by blue crater rims and fractured boulder faces. Brightening in the visible to near-infrared wavelengths follows, ultimately leading to more moderately blue spectral slopes, consistent with Bennu's average. The time scale associated with space weathering–induced color changes ($\sim 10^5$ years) is compatible with previous findings only if Bennu's small reddish craters formed under conditions in which gravity, rather than the strength of the impacted surface, is the dominant influence. This finding offers an indication of cratering physics on small rubble-pile asteroids. ■

The list of author affiliations is available in the full article online.
*Corresponding author. Email: danidg@lpl.arizona.edu

Cite this article as D. N. DellaGiustina *et al.*, *Science* **370**, eabc3660 (2020). DOI: 10.1126/science.abc3660

READ THE FULL ARTICLE AT
https://doi.org/10.1126/science.abc3660

RESEARCH ARTICLE

ASTEROIDS

Variations in color and reflectance on the surface of asteroid (101955) Bennu

D. N. DellaGiustina[1,2]*, K. N. Burke[1], K. J. Walsh[3], P. H. Smith[1], D. R. Golish[1], E. B. Bierhaus[4], R.-L. Ballouz[1], T. L. Becker[1], H. Campins[5], E. Tatsumi[6,7], K. Yumoto[7], S. Sugita[7], J. D. Prasanna Deshapriya[8], E. A. Cloutis[9], B. E. Clark[10], A. R. Hendrix[11], A. Sen[10], M. M. Al Asad[12], M. G. Daly[13], D. M. Applin[9], C. Avdellidou[14], M. A. Barucci[8], K. J. Becker[1], C. A. Bennett[1], W. F. Bottke[3], J. I. Brodbeck[1], H. C. Connolly Jr.[15], M. Delbo[14], J. de Leon[6], C. Y. Drouet d'Aubigny[1], K. L. Edmundson[1], S. Fornasier[8,16], V. E. Hamilton[3], P. H. Hasselmann[8], C. W. Hergenrother[1], E. S. Howell[1], E. R. Jawin[17], H. H. Kaplan[18], L. Le Corre[11], L. F. Lim[17], J. Y. Li[11], P. Michel[14], J. L. Molaro[11], M. C. Nolan[1], J. Nolau[4], M. Pajola[19], A. Parkinson[9], M. Popescu[20,6], N. A. Porter[1], B. Rizk[1], J. L. Rizos[6], A. J. Ryan[1], B. Rozitis[21], N. K. Shultz[1], A. A. Simon[18], D. Trang[22], R. B. Van Auken[1], C. W. V. Wolner[1], D. S. Lauretta[1]

Visible-wavelength color and reflectance provide information about the geologic history of planetary surfaces. Here we present multispectral images (0.44 to 0.89 micrometers) of near-Earth asteroid (101955) Bennu. The surface has variable colors overlain on a moderately blue global terrain. Two primary boulder types are distinguishable by their reflectance and texture. Space weathering of Bennu surface materials does not simply progress from red to blue (or vice versa). Instead, freshly exposed, redder surfaces initially brighten in the near-ultraviolet region (i.e., become bluer at shorter wavelengths), then brighten in the visible to near-infrared region, leading to Bennu's moderately blue average color. Craters indicate that the time scale of these color changes is ~10^5 years. We attribute the reflectance and color variation to a combination of primordial heterogeneity and varying exposure ages.

The near-Earth asteroid (101955) Bennu is the target of the OSIRIS-REx (Origins, Spectral Interpretation, Resource Identification, and Security–Regolith Explorer) sample-return spacecraft (*1*). Before launch, telescopic observations of Bennu had identified it as a low-albedo object—potentially indicating a carbon-rich composition—with a featureless, gently blue spectrum (blue signifies a negative spectral slope with respect to the solar spectrum, whereas red signifies a positive slope). This resulted in its classification as a blue (B-type) asteroid (*2*), a subclass of the broader carbonaceous (C-complex) group of small bodies. Bennu is a rubble-pile asteroid (*3*–*6*), accumulated from fragments of a larger parent body that was shattered by a catastrophic impact in the inner main asteroid belt ~1 billion years ago (*3*). Bennu eventually migrated from the main belt into its current orbit in near-Earth space (*3*).

OSIRIS-REx measurements acquired during the initial phases of the mission showed that Bennu is dominated by hydrated clay-bearing minerals (phyllosilicates) and magnetite (*7*), indicating that water was present on and altered the composition of Bennu's parent body (aqueous alteration). Organic compounds and carbonates have been discovered across the asteroid's surface, supporting the hypothesis that B-type asteroids are carbon rich (*8*, *9*). Carbon-bearing species are optically opaque (as is magnetite) and thus could be responsible for Bennu's low global normal albedo of 0.044 (*4*, *10*). These findings suggest that Bennu's composition may be representative of the primitive bodies that delivered water and organic molecules to early Earth (*11*).

Although the initial composition of an asteroid influences its global colors, physical properties such as particle size, surface roughness, and porosity can also influence these spectral characteristics, as can duration of exposure to the space environment. The surface colors of airless bodies are expected to be heavily altered by space weathering processes (*12*, *13*), including bombardment by solar wind particles and meteoroids. On anhydrous planetary surfaces, such as the Moon and stony (S-type) asteroids, space weathering darkens and reddens spectral slopes in the visible and near-infrared region (*12*, *14*). However, on primitive carbonaceous asteroids such as Bennu, and their meteorite analogs, space weathering effects are not well understood. Measured colors of primitive asteroids do not show consistent spectral relationships with surface exposure age (*13*, *15*–*17*), nor do laboratory experiments of simulated space weathering on analogous meteorite and phyllosilicate samples: Some studies indicate that space weathering leads to bluing (*13*, *18*–*22*), but others find that it leads to reddening (*16*, *20*, *23*, *24*). This is likely because the initial composition and the physical structure of the materials play a role in the spectral changes observed (*16*, *20*). To determine how space weathering affects low-albedo carbonaceous asteroids, we searched for a correlation between Bennu's colors and the age of its surface features determined from morphology. The spatial distribution and geologic setting of varying colors on Bennu may also aid our understanding of the composition and evolution of the asteroid's surface.

Color observations of Bennu

OSIRIS-REx obtained color observations of Bennu during two hyperbolic flybys on 14 March and 26 September 2019, as part of the Baseball Diamond campaign of the mission's Detailed Survey (*25*). The OSIRIS-REx Camera Suite (OCAMS) (*26*) acquired color images using the multispectral MapCam imager, which has four bands in the visible (VIS; 0.40 to 0.70 μm) and near-infrared (NIR; 0.70 to 2.5 μm) wavelengths. The MapCam bands—*b′* (0.44 to 0.50 μm), *v* (0.52 to 0.58 μm), *w* (0.67 to 0.73 μm), and *x* (0.82 to 0.89 μm)—are similar to those used by telescopic surveys (*27*) to infer asteroid composition and classify their spectra (*28*). Most asteroid observations have been limited to unresolved disk-integrated (globally averaged) spectra. We used spatially resolved MapCam color images (pixel scale ~25 cm) to investigate reflectance and color across Bennu's surface. To establish relationships between color and surface morphology, we paired these color observations with higher-resolution OCAMS PolyCam panchromatic images (2 to 5 cm per pixel) of the same locations.

We radiometrically calibrated the MapCam and PolyCam images to units of reflectance (also

---

[1]Lunar and Planetary Laboratory, University of Arizona, Tucson, AZ, USA. [2]Department of Geosciences, University of Arizona, Tucson, AZ, USA. [3]Southwest Research Institute, Boulder, CO, USA. [4]Lockheed Martin Space, Littleton, CO, USA. [5]Department of Physics, University of Central Florida, Orlando, FL, USA. [6]Instituto de Astrofísica de Canarias and Departamento de Astrofísica, Universidad de La Laguna, Tenerife, Spain. [7]Department of Earth and Planetary Science, University of Tokyo, Tokyo, 113-0033, Japan. [8]LESIA (Laboratoire d'Etudes Spatiales et d'Instrumentation en Astrophysique), Observatoire de Paris, Université PSL (Paris Sciences & Lettres), CNRS (Centre National de la Recherche Scientifique), Université de Paris, Sorbonne Université, 92195 Meudon, France. [9]Department of Geography, University of Winnipeg, Winnipeg, MB R3B 2E9, Canada. [10]Department of Physics and Astronomy, Ithaca College, Ithaca, NY, USA. [11]Planetary Science Institute, Tucson, AZ, USA. [12]Department of Earth, Ocean and Atmospheric Sciences, University of British Columbia, Vancouver, BC, Canada. [13]The Centre for Research in Earth and Space Science, York University, Toronto, ON, Canada. [14]Université Côte d'Azur, Observatoire de la Côte d'Azur, CNRS, Laboratoire Lagrange, Nice, France. [15]Department of Geology, Rowan University, Glassboro, NJ, USA. [16]Institut Universitaire de France (IUF), 1 rue Descartes, 75231 Paris CEDEX 05, France. [17]Smithsonian Institution National Museum of Natural History, Washington, DC, USA. [18]NASA Goddard Space Flight Center, Greenbelt, MD, USA. [19]Istituto Nazionale di Astrofisica (INAF), Osservatorio Astronomico di Padova, Padua, Italy. [20]Astronomical Institute of the Romanian Academy, Bucharest, Romania. [21]The School of Physical Sciences, The Open University, Milton Keynes, UK. [22]University of Hawai'i at Mānoa, Hawai'i Institute of Geophysics and Planetology, Honolulu, HI, USA.
***Corresponding author. Email: danidg@lpl.arizona.edu**

known as radiance factor or *I*/*F* (29). MapCam images were corrected to normal viewing conditions (0° solar incidence, 0° solar phase, and 0° observer emission angles) by using a Robotic Lunar Observatory photometric function to assess albedo differences across the surface (30, 31). We subsequently map-projected and mosaicked the MapCam images using cartographic techniques developed for irregular planetary bodies (23, 31, 32). Band ratios and principal components analysis (PCA) were used to identify variations in multispectral images and distinguish regions with distinct spectral properties (29). To establish statistically meaningful relationships between color, reflectance,

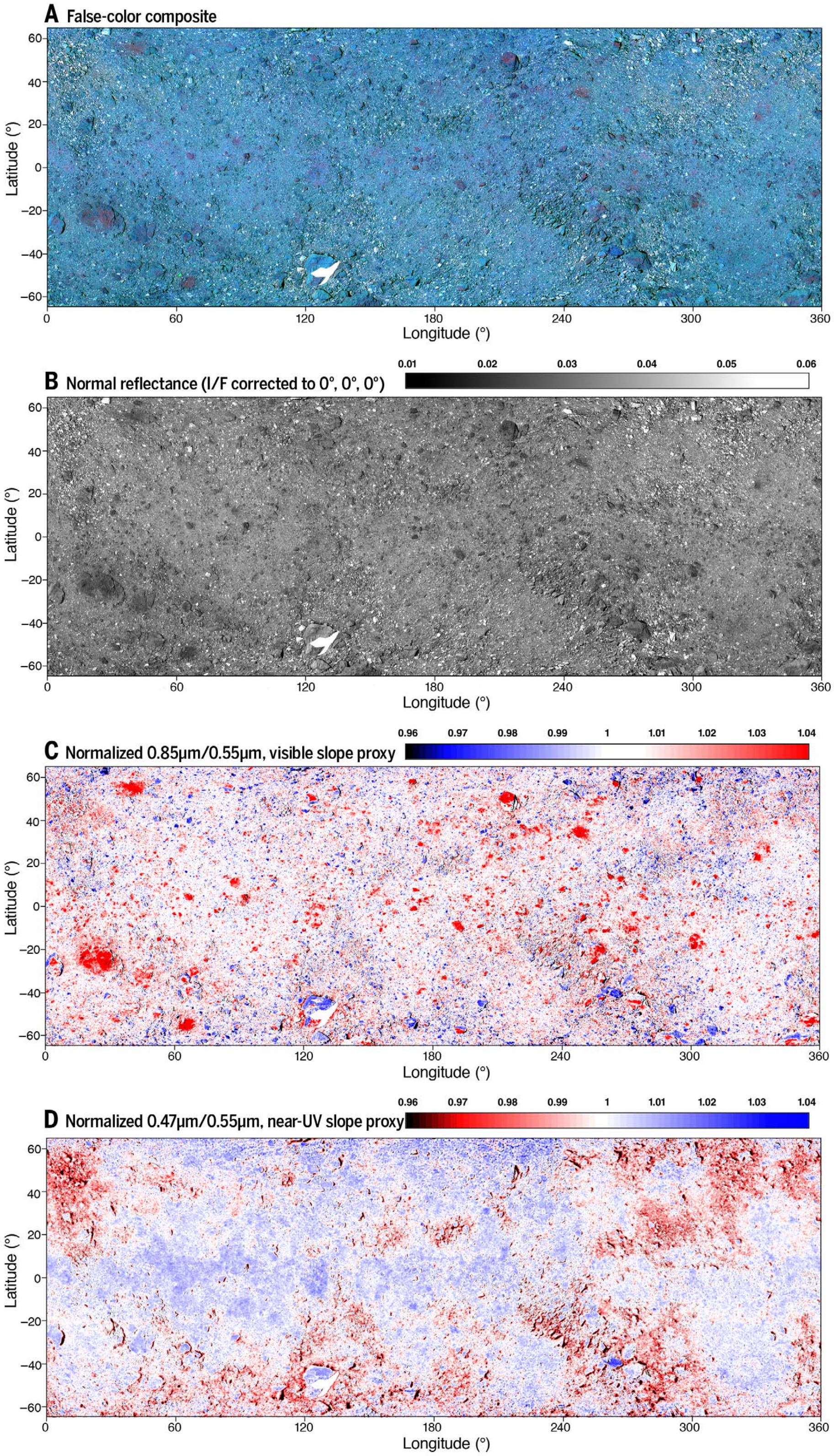

Fig. 1. Color composite, reflectance, and band ratio maps of Bennu. (**A**) False-color red-green-blue (RGB) color model composite overlaid on a 0.55-μm (*v* band) normal reflectance map of Bennu. Color channels are: red, *x*/*v* (0.85/0.55 μm, mid-VIS to NIR spectral slope); green, *w* band strength (depth at 0.70 μm, composition, fig. S5); and blue, *b*′/*v* (0.47/0.55 μm, near-UV slope). (**B**) Normal reflectance. (**C**) The *x*/*v* band ratio, a proxy for the mid-VIS to NIR spectral slope, where warmer values correspond to redder spectral slopes; values >1 are redder than the global average, and values <1 are less red than the global average. (**D**) The *b*′/*v* band ratio, a proxy for the near-UV slope, where higher values correspond to bluer spectral slopes; values >1 are bluer than the global average, and values <1 are less blue than the global average. All maps range from 65°N to 65°S latitude (positive and negative values on the *y* axes respectively correspond to north and south), 0° to 360°E longitude. The white area near 50°S, 128.5°E represents no data.

and morphological features, we mapped ~1600 boulders and ~700 craters, then extracted their median spectra using established methods (4, 31, 33). We assessed spectral variations that were bounded by irregular morphological features using centimeter-scale 3D digital terrain models produced with data from the OSIRIS-REx Laser Altimeter (OLA) (34–36). We also compared our findings with near-infrared hyperspectral data acquired at lower spatial resolution using the OSIRIS-REx Visible and InfraRed Spectrometer (OVIRS) (37).

Bennu's global photometric spectrum is moderately blue (*b*′ to *x* spectral slope of $-0.1701\ \mu m^{-1}$) in MapCam data (0.44 to 0.89 μm), but spectral

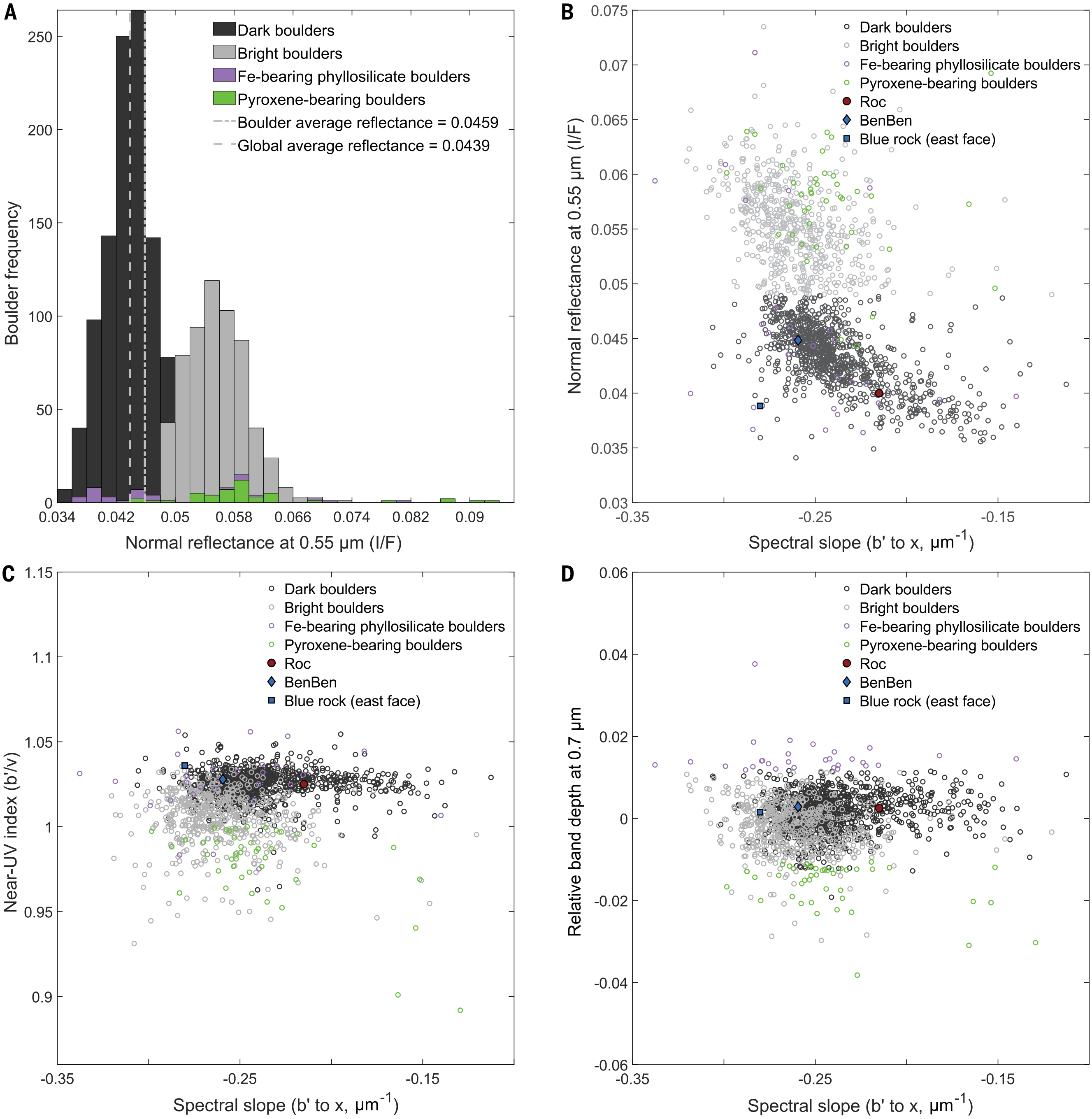

Fig. 2. Variation of boulder color and reflectance on Bennu. (**A**) Reflectance distribution of boulders (>5 m) on Bennu. The distribution is multimodal with more than one Gaussian component (31). Shading and colors indicate different classifications of boulders, as indicated in the legend. (**B**) Normal reflectance versus absolute spectral slope of the same boulder populations; some individual boulders are indicated in the legend. Dark boulders tend to be redder, and their reflectance monotonically decreases with increasing (redder) spectral slopes, whereas bright boulders are bluer and more scattered (31). (**C**) The near-UV index (*b*′/*v* band ratio) versus the *b*′ to *x* spectral slope. Dark boulders tend to have a steeper near-UV slope relative to the global average (>1), whereas bright boulders are more often spectrally flat or show a downturn in the near-UV (from the *b*′ to *v* bands). (**D**) The relative band depth at 0.7 μm (*w* band) versus the *b*′ to *x* spectral slope. Some boulders show an absorption feature at 0.7 μm (relative *w* band depth >0), indicative of Fe-bearing phyllosilicates. The boulders named Roc (23.6°S, 25.3°E; Fig. 3C) and BenBen (46.8°S, 127.5°E) are two of the largest on Bennu; both are dark. The blue rock (39.80°S, 263.02°E) is shown in Fig. 3E.

slopes vary from blue (negative, –0.25 μm^{-1}) to red (positive, 0.05 μm^{-1}) at spatial scales of as small as 2 m (Fig. 1). Bennu's surface exhibits widespread heterogeneity in reflectance (Figs. 1 and 2). PCA shows that the first principal component (PC1) corresponds to albedo, whereas the second principal component (PC2) corresponds to changes in the overall spectral slope (from b' to x), and PC3 indicates variation in the near-ultraviolet (near-UV) region (from b' to v) (figs. S1 to S3).

Bennu's globally blue surface is dominated by a coarse layer of decimeter- to meter-scale rocks with some centimeter-scale particles (regolith), which we refer to as average terrain. The spectral variability is associated with distinct geologic features, including boulders, craters, and areas of mass wasting (rock movement down geopotential slopes), which we used to distinguish color units on the asteroid (Table 1 and fig. S4, A and B). These units provide a framework for classifying commonly observed features on the surface.

Table 1. Adopted color units on Bennu and their distinguishing properties.

Color unit	Distinguishing properties
Bright boulders	Normal reflectance ranges from 0.049 to 0.074. Bluish spectral slopes are slightly steeper than the global average in the mid-VIS to NIR wavelengths (0.52 to 0.96 µm) but are often spectrally flat or show a downturn in the near-UV wavelengths (0.44 to 0.50 µm; MapCam *b′* band). Diameters are <10 m.
Dark boulders	Normal reflectance ranges from 0.034 to 0.049, overlapping with the average reflectance of Bennu (0.044). Slopes tend to be redder in the mid-VIS to NIR wavelengths (0.52 to 0.96 µm) and often show an upturn in the near-UV wavelengths, consistent with the global average. Diameters range from decimeters to ~95 m.
Fe-bearing phyllosilicate boulders	An absorption feature is present at 0.70 µm (determined from a relative band depth >1% in the MapCam *w* band). Reflectance spans a wide range, most often overlapping with that of dark boulders.
Pyroxene-bearing boulders	An absorption feature is present beyond 0.89 µm (determined from a downturn in the MapCam *x* band relative to the *w* band) due to pyroxene (36). Reflectance may reach up to 0.26 (36). These units can occur as discrete boulders or pyroxene-bearing clasts in a dark boulder–like matrix.
Blue units	These boulders and craters show an upturn in the near-UV wavelengths that exceeds that of the global average photometric spectrum, possibly resulting from an absorption at 0.55 µm.
Reddish craters	These small (<25-m diameter) craters are ≥0.5σ redder than Bennu's global average (median) and contain material that is not resolved at ~2 cm per pixel.
Breccias	These medium (~5 m) to large (>10 m) boulders have embedded clasts (tens of centimeters) whose spectrophotometric properties are distinct from those of the host matrix, which resembles the dark boulders.
Average terrain	These areas are absent of large boulders (≳20 m) and have a photometric spectrum similar to the global average (median).

Boulders on Bennu

Boulders are the primary source of heterogeneity on Bennu. Some individual boulders have VIS-NIR absorption features at 0.55 µm [as previously observed (5)], 0.7 µm (Fig. 2D), and near 1 µm [as previously observed (38)]. There are also outliers among the boulder population that do not correspond with a specific color unit.

Boulders have a wide range of normal reflectance values [0.032 to at least 0.26 (38)] that are multimodally distributed with two prominent peaks (Fig. 2A). The reflectance of boulders is not normally distributed and is most consistent with four Gaussians (31), or perhaps two or more non-Gaussian components. We refer to boulders as bright or dark based on whether they are brighter or darker than the median reflectance of 0.049, which lies between the two prominent peaks of the reflectance distribution.

Bright boulders have smooth surfaces, typically angular shapes (Fig. 3, A and B), and blue spectral slopes in the mid-VIS to NIR (MapCam v to x bands). However, unlike the average terrain, ~80% of the bright boulders are dark in the near-UV region ($b'/v < 1$; Fig. 2 and fig. S4, A and B). The bright boulders appear to have similar sizes (are well sorted) with diameters <10 m.

Dark boulders (reflectance ≤0.049) span a range of visible spectral slopes but are generally redder than the bright boulders in the mid-VIS to NIR wavelengths (Figs. 1 and 2, A and B). The dark boulders are less angular than bright boulders and commonly have rougher, more undulating surface textures (Fig. 3, C and D). They encompass a wide range of sizes (from decimeters to ~95 m) and include all large (≳20 m) boulders on the asteroid. Although the average terrain lies between the bright and dark populations, dark boulders and smaller dark particles (presumably formed by boulder breakdown) appear to be the dominant material; this is illustrated by the close correspondence between Bennu's average reflectance (0.0439 ± 0.002) and the reflectance peak of the dark boulder population (0.0450 ± 0.002) (Fig. 2A, gray dashed line).

Color variation is also evident within individual boulders (Figs. 1 and 3). Sometimes this occurs between faces of an individual rock, usually a large dark boulder (Fig. 3, C to H). These examples of intraboulder color variation are associated with apparent exfoliation and fracturing of the rock (39) (Fig. 3, G and H) and occur in textures akin to weathering rinds—exterior crusts that appear discolored compared with faces that are potentially more recently exposed (Fig. 3, C and G). We also observed boulders that appear to be breccias—that is, objects composed of rock fragments cemented together as a result of large impacts on Bennu's parent body (33, 38). In these boulders, spectrophotometrically distinguishable fragments (clasts) are embedded in a host matrix that has similar texture, reflectance, and color to the dark boulders (Fig. 3, E and F).

A small population of boulders with very high reflectance [up to 0.26 (38)] shows evidence of an absorption feature at 1 µm (downturn in

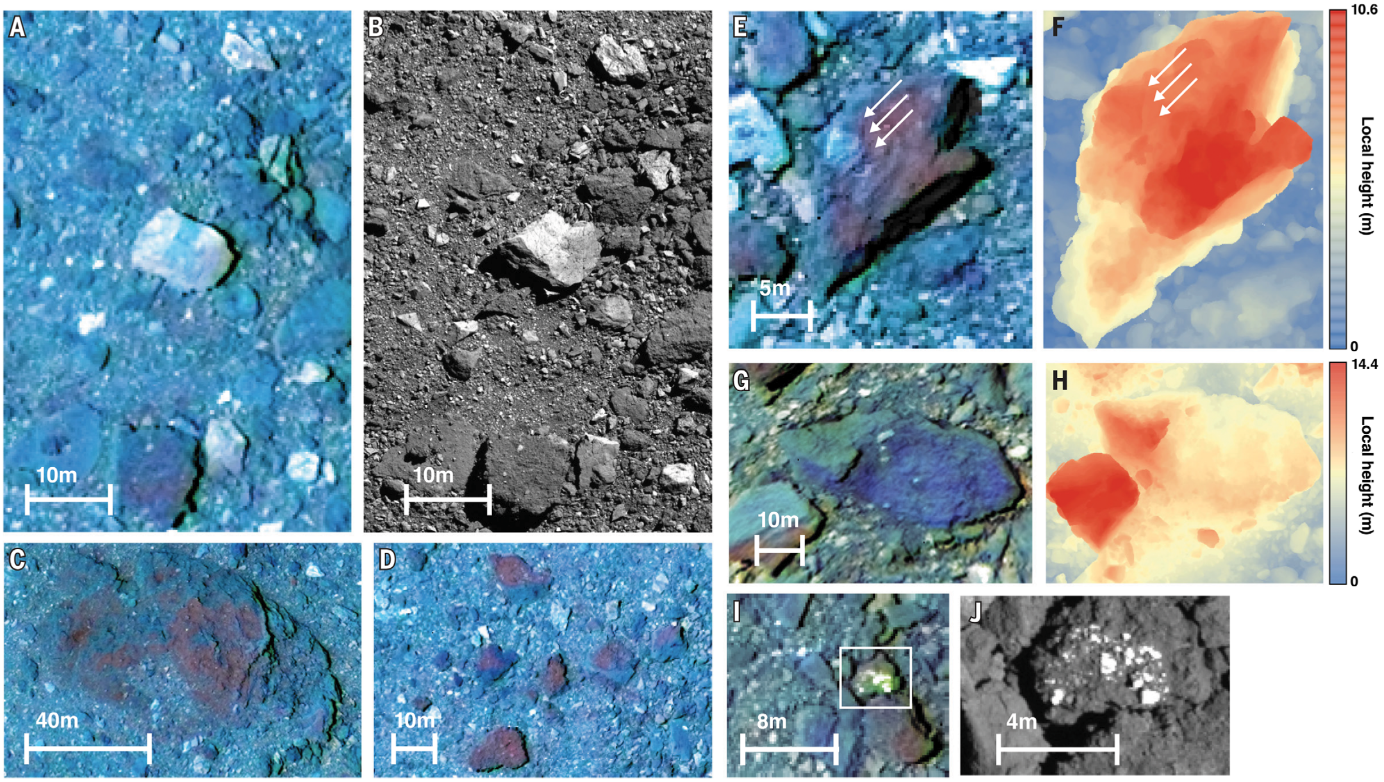

Fig. 3. Examples of boulder color and morphology. All RGB color composite images are shown on the same color scale as in Fig. 1A. (**A** and **B**) Bright boulders near 17.76°S, 74.74°E in (A) MapCam (25 cm per pixel) and (B) PolyCam (5.25 cm per pixel) images. The higher-resolution panchromatic PolyCam image (B) shows the angular morphology of bright boulders. (**C** and **D**) Dark boulders near (C) 23.6°S, 25.3°E and (D) 3.92°N, 178.98°E, some of which display intraboulder color variation. This includes Roc (C), which is the largest boulder observed on Bennu at 95 m in the longest observable dimension. (**E**) A dark boulder with resolvable clasts that appear distinct from the host matrix (4.62°S, 248.95°E). (**F**) Digital terrain model of the same boulder. The three arrows highlight the same clast in (E) and (F). (**G**) A rock at 39.80°S, 263.02°E. The darker and bluer portion corresponds to a lower-relief fractured face in the digital terrain model (**H**). (**I**) A boulder that appears to contain clasts and be brecciated; the bright clasts with a greenish color signature are indicative of pyroxene in this false-color scale. (**J**) A higher-resolution PolyCam image (5.25 cm per pixel) of the same boulder. A wider context image is shown in fig. S15.

the x band). OVIRS data indicate that these boulders contain pyroxene (*38*). Pyroxene-bearing material appears in distinct clasts embedded within larger host rocks whose color and reflectance are similar to those of the dark boulders (Fig. 3, I and J) (*38*); it also appears in smaller (meter-scale), isolated boulders that do not look brecciated. Pyroxene was probably inherited from Bennu's parent body, where it was implanted by an impactor that may have originated from a fragment of (4) Vesta (*38*), the differentiated (not primitive) inner–main-belt asteroid visited by the Dawn mission (*40*). Although their reflectance overlaps with that of the bright boulders and their texture is like that of the breccias, we separated pyroxene-bearing boulders into their own category (Table 1) based on their distinct spectral shape in the VIS to NIR (v to x; Fig. 2, B and C).

Some boulders have an absorption feature at 0.7 μm (absorption depth of 2 to 10%). Similar absorption features have been observed in spectra of primitive asteroids and carbonaceous meteorites, where they were attributed to iron in some clay-bearing phyllosilicates (*41*). Boulders with the deepest absorptions at this wavelength span a wide range of reflectance (0.036 to 0.081); however, most (~60%) dark boulders tend to have a shallow (~1%) 0.7-μm absorption. Although this is at the limit of the 1% relative precision of OCAMS data (*29*), it is spatially coherent with individual boulders, giving us confidence that the feature is real (fig. S5).

Color and surface processes

Some areas of the surface are brighter in the near-UV region (i.e., show an upturn in the near-UV b' band; $b'/v > 1.01$, or 1% greater than average); we refer to these areas as blue units. One of the bluest contiguous surfaces on Bennu is the eastern side of the boulder shown in Fig. 3G. Digital terrain models show that this rock face is recessed relative to the western face of the boulder (Fig. 3H), and color data indicate that the recessed face has a steeper blue spectral slope. Conversely, the western face of the boulder is brighter and has a more neutral spectral slope, similar to the global average (fig. S4C). The bluer, recessed eastern face may be a fresher surface, more recently exposed to the space environment by thermal fracturing or exfoliation—ongoing surface processes on Bennu (*39*, *42*). Similar patterns are observed on other boulders that appear to have been recently exfoliated (as indicated by layers with different relief). We also observe bluer-than-average near-UV slopes on the high-elevation rims (10 to 20 m higher than surrounding terrains) of equatorial craters that show recent indications of mass wasting (Fig. 4, A and B) (*43*).

The correspondence between blue units and potentially less weathered surfaces suggests that enhanced near-UV reflectance is related to younger exposure ages on Bennu. The blue units are correlated with the relative band depth at 0.55 μm (fig. S6), indicating that the upturn observed in the near-UV index may be the result of an absorption feature at 0.55 μm. This absorption feature on Bennu has previously been attributed to magnetite (*5*), which is also detected in thermal emissivity spectra from the OSIRIS-REx Thermal

Emission Spectrometer (OTES) (*7*). However, this absorption feature could also result from graphitized carbon (*44*), and both magnetite and graphite are associated with space weathering (discussed further below).

The color of the largest craters (>100 m) on Bennu is indistinguishable from that of the average terrain. However, many small craters (≤25 m) are redder than Bennu's average by $\geq 0.5\sigma$ in the near-UV to NIR, where σ is the full-width at half maximum of the global distribution of b' to x spectral slopes (Figs. 4, C and D, and 5, A and B). We refer to these as small reddish craters. By contrast, we identified no craters bluer than Bennu's global average spectral slope by $\leq 0.5\sigma$ (Fig. 5A).

The size-frequency distribution of reddish craters implies that they are one of the youngest components of the global crater population (Fig. 5C). If so, we expect that reddish craters are among the youngest surface features on Bennu. The absolute spectral slopes of the reddish craters appear to correspond with crater size (Fig. 5, A and B), and these craters are also darker than the global average (Fig. 5D). In PolyCam images, the reddish craters display a texture distinct from that of the bulk of Bennu's surface: unresolved at the pixel scale (i.e., <5 cm), indicating fine-particulate material (fig. S7). The largest examples of reddish craters exist at mid- to high latitudes (poleward of ±20°), including the crater selected as the primary OSIRIS-REx sample collection site, Nightingale (56°N, 42°E).

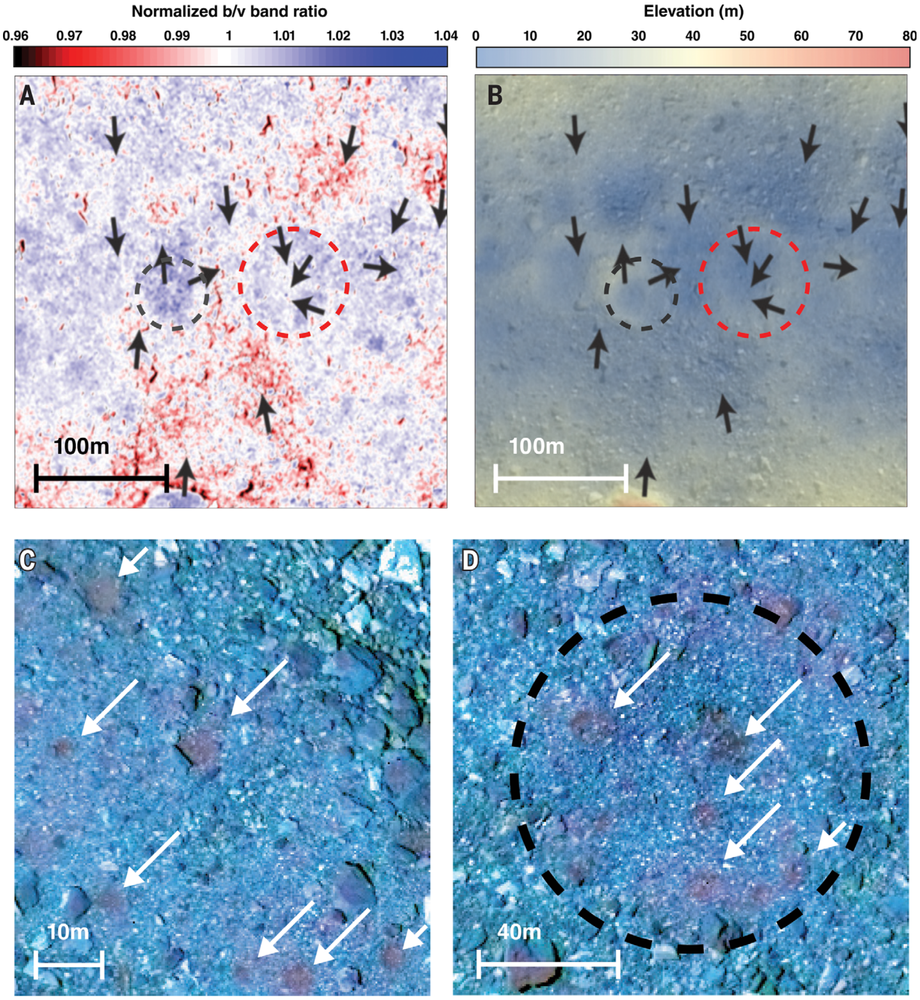

Fig. 4. Examples of crater color. (**A**) The b'/v band ratio map of equatorial craters at 3.05°S, 128.79°E (black dashed circle) and 1.06°S, 152.75°E (red dashed circle), which have a relatively high near-UV index and are considered blue units. (**B**) An elevation map of the same equatorial craters in (A). These blue units correspond with areas that show recent indications of mass movement away from regionally high elevations, such as from crater rims. Black arrows correspond to locations of previously mapped mass movement (*43*). (**C** and **D**) RGB color composite images of small craters (indicated by white arrows), shown on the same color scale as in Fig. 1A. As indicated by their color, these craters are consistently redder than Bennu's average terrain, with positive to slightly blue b' to x spectral slopes. The blue crater indicated by the dashed black circle in (A), (B), and (D) has been overprinted by several smaller reddish craters.

Evidence of freshly exposed material on Bennu

Reddish craters and blue units on Bennu both correspond to apparently young exposure ages (Figs. 3, G and H, and 4, C and D). To resolve this apparent contradiction, we considered crater production rates and size-scaling laws, stratigraphic relationships, and potential contributors to spectral slopes other than exposure age.

The size-frequency distribution of the reddish craters has a power-law index of –2.1 ± 0.4 (*31*). The power-law index of the reddest subset of these craters (b' to x spectral slopes $\geq 1\sigma$ from the global median value, i.e., $\geq -0.0698\ \mu m^{-1}$) is –2.3 ± 0.6 (*31*). These values are close to that of the expected production of craters in the present-day main asteroid belt and near-Earth space over the past 100,000 years (predicted power-law index between –2.6 and –2.7; Fig. 5C) (*45*–*48*). The global crater population has a different power-law index of –1.1 ± 0.1 (*31*). At small diameters, the distribution of the reddish craters does not deviate from that of the expected crater production (Fig. 5C), unlike the global population of craters on Bennu (*33*) and nearly all other closely studied small bodies (*49*). A mismatch at small diameters between observed crater populations and the expected crater production has been attributed to erasure processes (*49*), which efficiently erode and diminish small craters. The correspondence between the expected production of the redder craters on Bennu and their actual distribution supports a young age: Unlike the global crater distribution, they have not yet experienced substantial erasure.

We estimated the time required to produce the craters on Bennu using a crater production rate and a scaling law for crater size from impactor size (*31*). Assuming that the redder craters have formed since Bennu's arrival in the inner Solar System, we adopted the established crater production rate from the near-Earth object population (*47*, *48*). Crater scaling relationships, however, are less certain owing to unknown material properties and the structure of rubble-pile asteroids. The Small Carry-on Impactor (SCI) experiment performed on asteroid (162173) Ryugu by the Hayabusa2 mission (*50*) showed that small impactors (~30 cm) can produce craters consistent with scaling laws that depend on gravity; craters formed in this gravity regime can be many times larger than the sizes expected from scaling laws governed by target material strength. The sizes of the reddish craters on Bennu are smaller than or similar to the diameter of the SCI crater (~18 m) (*50*). If gravity dominates the cratering process for small craters on Bennu (*51*), the reddest subset of these craters is less than 10^5 years old

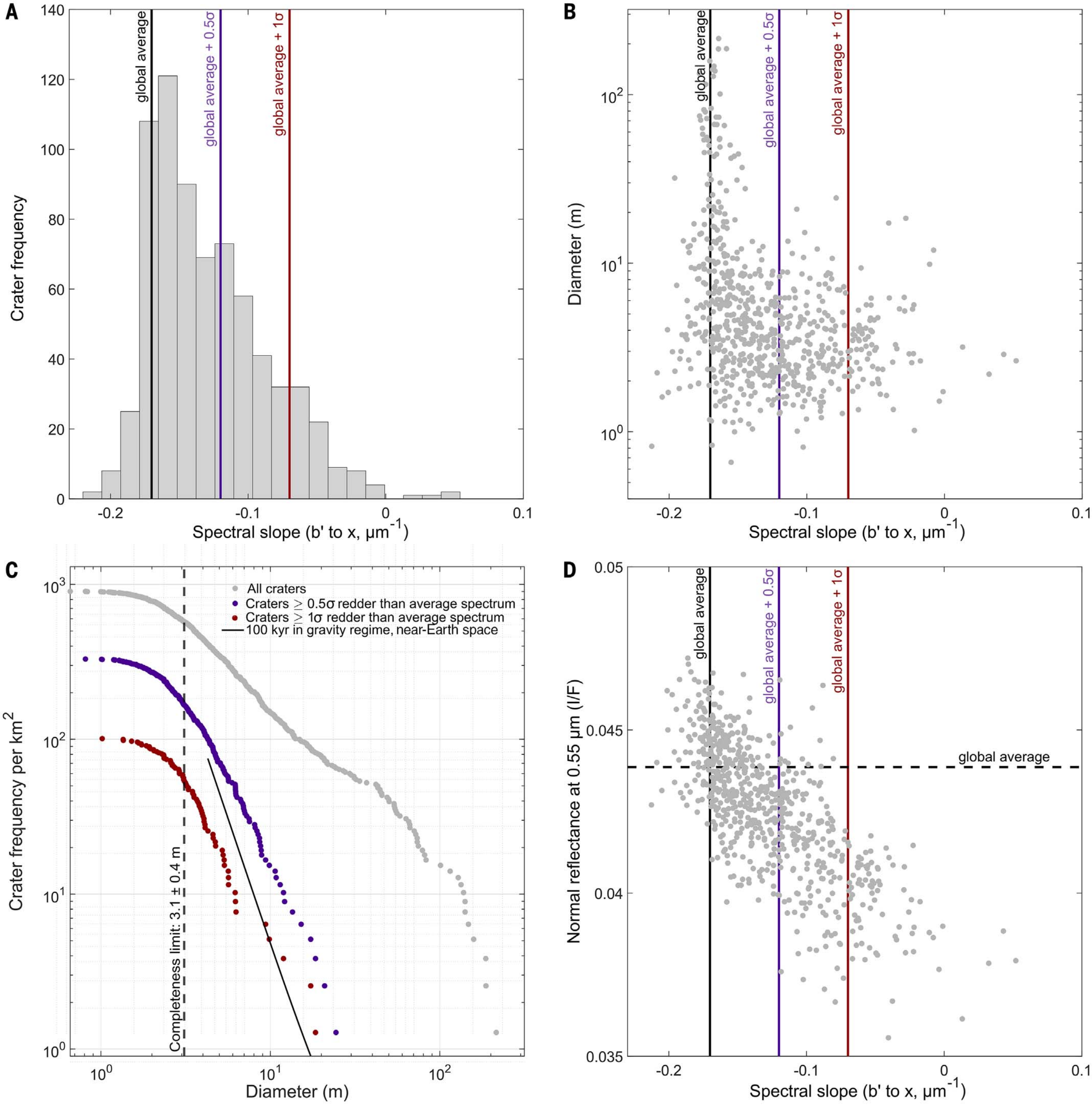

Fig. 5. Color, reflectance, and size distribution of Bennu's craters. (**A**) The *b'* to *x* spectral slope distribution of craters on Bennu, which are not normally distributed. (**B**) Crater diameter as a function of the crater's median *b'* to *x* spectral slope. Craters have more negative spectral slopes at higher size and frequency; this suggests that redder (more positively sloped) craters are younger. (**C**) The crater size frequency distribution on Bennu for craters classified on the basis of their *b'* to *x* spectral slopes. The black line shows the expected crater production for 100,000 years in near-Earth space (cumulative power-law index of –2.7), assuming cratering in the gravity regime (*51*). The size-frequency distribution of the reddish craters (purple circles) is more consistent with the black line at small diameters than that of the global crater population (gray circles). The reddest subset of craters (red circles) falls below the black line and appears to have formed more recently than 100,000 years ago. (**D**) The normal reflectance of craters on Bennu as a function of *b'* to *x* spectral slope. Like that of dark boulders, the reflectance of craters monotonically decreases with increasing (redder) spectral slopes (*31*). Supporting information for the relationship between spectral slope and crater size and frequency is shown in fig. S16.

(Fig. 5C). This is consistent with the expected time scale of space weathering on near-Earth asteroids (~10^5 years) based on returned samples of asteroid Itokawa (*52*) and laboratory experiments on primitive meteorites (*20*). Thus, it is plausible that the reddish craters are the most recent areas of surface exposure and represent the least weathered material on Bennu.

Although recent surface exposure may explain the reddish craters on Bennu, in carbonaceous meteorites, redder spectral slopes in the VIS-NIR can also arise from fine particle sizes (<100 μm) (*53*). The smooth and unresolved appearance of the reddish craters on Bennu suggests that they possess finer-scale regolith (fines) than elsewhere on the surface (fig. S7). However, small craters on boulders also appear redder than the global average photometric spectrum, indicating that particle size is not the only factor (fig. S8). When the electrostatic forces acting on particles exceed that of gravity and cohesion—as is often the case for micrometer-sized grains on asteroids—lofting occurs and preferentially removes fines (*54*). Simulations of electrostatic lofting show that detachment and escape of submillimeter particles is feasible on Bennu and likely occurs shortly after the formation of such fines (*54*). Although particle sizes <100 μm could contribute to reddening on Bennu, we anticipate that the loss of fines takes place on shorter time scales than the age of the reddish craters. However, if micrometer-scale particles are closely associated with freshly exposed materials, they could also produce the observed reddening.

Longer infrared wavelengths also indicate younger exposure ages for reddish craters. The shape of the 2.7-μm hydration feature, which is ubiquitous on Bennu (*7*), is sharper and shifts to shorter wavelengths within reddish craters, including the Nightingale sample site (fig. S9A). This is consistent with laboratory space weathering experiments performed on carbonaceous meteorites (*20*), which show that the minimum of the hydration feature at ~2.7 μm moves toward longer wavelengths with prolonged exposure to space weathering processes. Thus, sharper band features with shorter minimum wavelengths within craters may signify more recent exposure. The blue equatorial crater at 1.06°N, 152.75°E (Fig. 4, A and B) appears to have a sharper absorption feature but a band minimum similar to the global average (fig. S9B), indicating that it may have an intermediate exposure age. Unlike the spectral slope, the shape of this spectral signature is not expected to be influenced by particle size (*20*).

The exposure age is less clear for the bluer-than-average, apparently broken boulder face in Fig. 3, G and H. We can set some constraints from the blue units associated with equatorial craters. Since its time in near-Earth space, Bennu's rotation rate has accelerated in response to surface scattering of sunlight and the emission of its own thermal radiation (*10*, *55*), consequences of the Yarkovsky-O'Keefe-Radzievskii-Paddack (YORP) effect. The locations of two of the bluest craters (1.06°S, 152.75°E and 3.05°S, 128.79°E) correspond to an isolated equatorial region that experienced increased surface accelerations as Bennu's spin period decreased from 5 hours to the present-day 4.3 hours (fig. S10) (*10*, *55*), suggesting that this area has experienced surface mass movement at some point in the past 200,000 years (*43*). Thus, we infer that the exposure age of blue units is ~200,000 years.

Blue unit craters have also been overprinted by small reddish craters (Fig. 4D); we therefore presume that they are composed of the same underlying material and that the blue unit craters are older than the reddish craters. This color trend of bluing with exposure time is consistent with some spectral studies of space weathering of carbonaceous meteorites (*18*–*22*) but not previous surface-resolved observations of asteroids.

We suggest that nonlinear space weathering occurs on Bennu's surface. In this scenario, freshly exposed material is initially redder than the bulk of Bennu in the near-UV to NIR wavelengths (b' to x) (first stage). During early space weathering, these surfaces brighten more rapidly in the near-UV (b') than in the mid-VIS to NIR (v to x), thereby increasing the b'/v band ratio (middle stage). This near-UV bluing may result from the deepening of an absorption near 0.55 μm, implying that magnetite or graphite abundance increases during the early stages of space weathering. Eventually, however, these color differences neutralize as the surface is brightened across the wavelengths observed by MapCam, and the downturn at 0.55 μm (v band) diminishes, leading to the gently blue spectral slope that characterizes Bennu's global photometric spectrum and the oldest craters (final stage).

This space weathering progression is demonstrated by craters that have been categorized on the basis of their spectral slope (Fig. 6). The first and middle stages are illustrated by the small reddish craters overprinted on blue equatorial craters (Fig. 4D). The middle and final stages may also be illustrated by the boulder in Fig. 3G, whose higher-relief, presumably older western face is brighter and has a more neutral spectral slope than the more recently exposed, bluer face. The final stage is illustrated by Bennu's average terrain.

The orientation of intraboulder color variation provides further evidence of space weathering on Bennu. We examined 220 boulders with sizes ≳5 m in the equatorial region (20°S to 20°N), where MapCam images have the most consistent viewing conditions, and calculated the azimuthal angle that maximizes blue-to-red color variation across each boulder (*31*). Figure S11 shows the latitude of boulders with large color variation (b' to x slope difference of $>0.05\ \mu m^{-1}$ between the two regions) as a function of the azimuthal angle of the blue-to-red direction (*31*). Bluer faces are preferentially oriented toward the equator (fig. S12). This may relate to solar exposure (e.g., heating or irradiation) and/or meteoroid bombardment, all processes that would preferentially affect equatorial latitudes (*42*, *56*). We observed this intracolor variation only on dark boulders, perhaps owing to their larger sizes compared with other boulder types, or a different initial composition.

Mechanisms for space weathering on Bennu

Dark, optically opaque minerals, such as nanophase iron, graphitized carbon, sulfides, and magnetite, are commonly produced by space weathering of primitive materials (*19*, *23*, *44*, *57*). Laboratory studies have shown that phyllosilicates intimately mixed with certain carbon species (including graphite) and magnetite can lead to bluer and darker spectral slopes in the visible wavelengths (*44*) (fig. S4, C and D). The link between bluing opaque minerals and space weathering implies that blue spectral slopes are the result of a mature, weathered regolith on primitive B-type asteroids, although they cannot fully explain the brightening in the near-UV to NIR observed on Bennu.

As discussed above, studies of primitive asteroids and meteorites have contradictorily predicted both bluing and reddening with increased space weathering (*13*–*24*). Ion and meteoroid bombardment lead to darkening and reddening of anhydrous silicate planetary surfaces; this has previously been attributed to the accumulation of nanophase and larger metallic iron particles, which form in response to the space environment (*58*). However, contrary to the bluing and darkening predicted from the production of graphitized carbon and magnetite, the formation of nanophase iron in low-albedo asteroids such as Bennu may have a reddening and brightening effect, owing to the higher reflectance of nanophase iron than that of the primitive materials found in carbonaceous meteorites (*59*).

Space weathering trends observed on Bennu corroborate earlier studies (*13*, *44*) that found that primitive asteroids, though dark relative to the asteroid population, are brighter in the UV than their primitive meteorite counterparts—that is, they are spectrally bluer at shorter wavelengths. Ion bombardment of primitive low-albedo meteorites in the laboratory leads to spectral bluing and brightening (*20*). These spectral changes are attributed to the process of carbonization, whereby hydrogen is lost and crystalline carbon structures, such as graphite, are formed (*57*). Irradiation experiments on complex hydrocarbons have shown that carbonization can induce metal-like optical properties in carbonaceous material, which leads

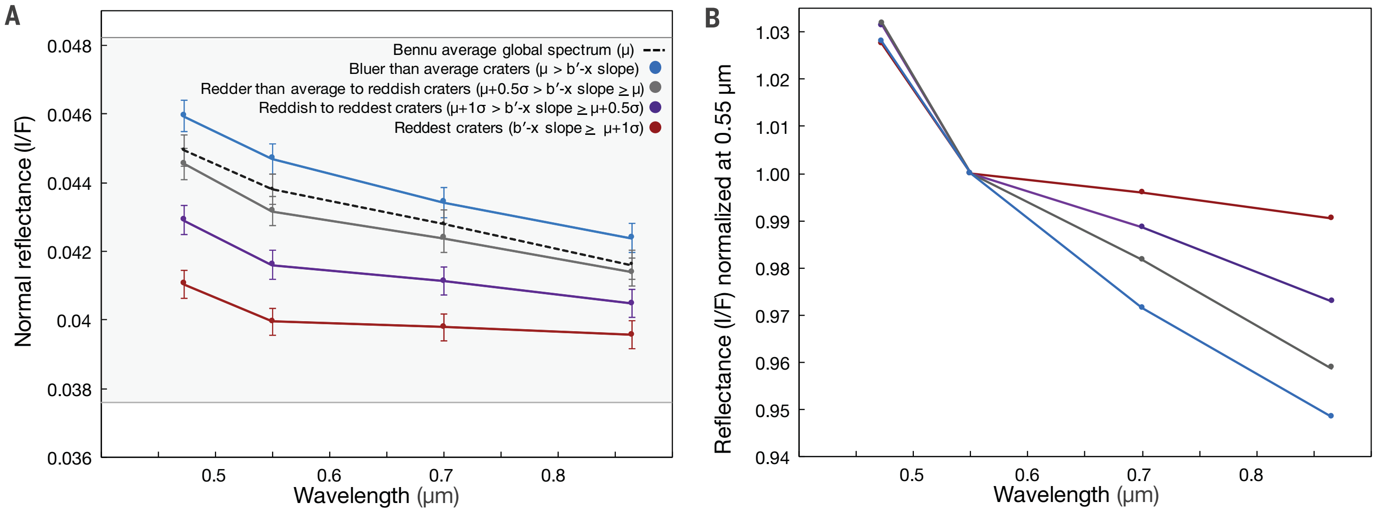

Fig. 6. Evolution of crater colors from MapCam data. Older craters have bluer overall spectra from *b*′ to *x* (Fig. 5); here we show variations in each filter separately. (**A**) The average absolute reflectance spectra of all craters within a given *b*′ to *x* slope range (see Fig. 5A). The light gray box encompasses the range of absolute radiometric uncertainty (*29*), whereas error bars show the relative precision of OCAMS measurements (*26*). Craters become brighter as their spectral slopes steepen. (**B**) The same reflectance spectra shown in (A), normalized at 0.55 μm. The progression from the mid-VIS to NIR (*v* to *x* bands) dominates the evolution of crater spectra, which mature toward more negative slopes. In the near-UV, spectra with intermediate *b*′ to *x* slopes steepen in a subtle but statistically significant way (*31*). This may result from more rapid brightening in the near-UV relative to longer wavelengths, a deepening of absorption feature at 0.55 μm (*v* band), or both. As a result, crater spectra show a non-unidirectional change near the *b*′ band as they age.

to bluing and brightening (*17*, *57*). We propose that space weathering–induced carbonization or magnetite formation may have influenced the surface colors on Bennu, especially in dark materials that become bluer (from the *v* to *x* bands) and brighter (across all bands) with increased exposure age.

Evidence for parent body heterogeneity

Although space weathering may influence the spectral slopes on Bennu, the disparate boulder populations that we identify—which differ in terms of their reflectance, texture, and size—suggest that some of Bennu's heterogeneity was inherited from its parent body. Dark boulders show a monotonic relationship of decreasing reflectance with increasing (redder) spectral slope, which is distinguishable from that of their bright counterparts (Fig. 2B) (*31*). Because space weathering is likely controlled by initial texture and composition, the difference in spectral slope trends between dark and bright boulders could result from the maturation of geologically distinct materials. Likewise, the less varied spectrophotometric properties of the bright boulders suggest that they are less susceptible to modification from space weathering or change on a different time scale (Fig. 2).

Heterogeneity in boulder reflectance on Bennu may be the result of distinct rock types that fragment differently, leading to an observed difference in their size-frequency distributions (*4*). Different compositions of the dark versus bright boulders may account for the correlation between reflectance and thermal properties for boulders on Bennu (*60*). The dark boulders have lower thermal inertia, which is attributed to higher porosity (*60*), consistent with their rougher and more crumbly (friable) appearance (Fig. 3, C and D). Conversely, the apparently smoother, more consolidated and angular bright boulders (Fig. 3, A and B) tend to have higher thermal inertias, attributed to lower porosity (*60*). Distinct texture and porosity can follow from differing mineralogy, levels of compaction, or heating and aqueous alteration histories.

The average blue spectrum of Bennu is consistent with serpentine or magnetite and serpentine, with some carbon (fig. S4, C and D). This composition is similar to that of Bennu's presumed meteorite analogs, the CM and CI groups of carbonaceous chondrites, which are dominated by Fe- and Mg-bearing phyllosilicates, respectively. In the most intensely aqueously altered CI chondrites, the Fe is contained in oxides, sulfides, carbonates, and other minor species (*61*–*63*).

The tendency of dark boulders to be slightly redder and brighter in the near-UV region (Fig. 2, A to C) may indicate that they have a higher overall abundance of organic molecules compared with their bright counterparts. This composition manifests as lower reflectance and redder slopes in more freshly exposed surfaces, which develop into steeper blue slopes during the early stages of space weathering. This, along with the weak 0.7-μm absorption sometimes present in dark boulders (Fig. 2D), is indicative of a higher proportion of Fe-bearing phyllosilicates than other boulders and implies that they represent a population of material from Bennu's parent body that has experienced less aqueous alteration. A correlation between lower reflectance and a 0.7-μm absorption band is consistent with moderately altered CM carbonaceous chondrites, which are among the darkest primitive meteorites with a nearly ubiquitous 0.7-μm absorption feature (*64*).

Some bright boulders contain veins of brighter material, which may be composed of carbonates (*9*). This implies a level of aqueous alteration that should also lead to the formation of magnetite (*65*). The lack of a near-UV upturn in carbonate-bearing boulders could signify that other phases influence their spectral characteristics. For example, bright boulders may be dominated by a hydrated mineral that is more absorbing at the longer wavelengths (so the reflectance is bluer).

We expect vein-bearing boulders to contain less organic material if their reduced carbon was oxidized by fluids to form the observed carbonates (*66*). Thus, if both low albedo and near-UV bluing are caused by the carbonization of organics via space weathering, we expect those spectrophotometric effects to be weaker in the vein-bearing rocks—as is observed (Fig. 2, A and C). Although graphitized carbon could explain the bluing observed in the more recently exposed faces of dark boulders, a UV upturn is also consistent with increasing abundances of magnetite, which has a blue spectral slope shortward of 0.5 μm (*65*).

The presence of potential carbonate veins (*9*) in bright boulders signifies a greater degree of aqueous alteration than in their dark counterparts, suggesting an origin within the interior of Bennu's parent body. In dark boulders, we do not find a clear spectral signature indicative of their provenance; however, their textures may provide clues. Brecciated boulders typically have a host matrix similar in texture to the dark boulders, including examples with clasts of exogenic pyroxene; this implies that these rocks formed near the surface of Bennu's parent body (*38*). Boulders on Bennu thus may have originated from different zones within the parent body. The multimodal distribution of the boulder populations implies that different processes (or extents of processes), such as aqueous alteration and heating, led to their distinct spectrophotometric properties.

Comparison with Ryugu

Asteroid Ryugu, visited by the Hayabusa2 spacecraft, is also a low-albedo, carbonaceous near-Earth asteroid. Although both asteroids are thought to have come from primitive asteroid families in the inner main belt (*67*), Ryugu, unlike Bennu, appears to have experienced partial dehydration (*68*). The multiband cameras onboard the two spacecraft use similar photometric filters in the visible wavelengths and thus allow a direct comparison of the spectra from each (*26*, *31*, *68*). Figure S13 shows the areal distribution of the reflectance and near-UV to NIR spectral slope of each asteroid. The variation in reflectance on Bennu is 1.7 times that on Ryugu, and Bennu exhibits a bluer overall color. Though the standard deviations of the spectral slope distributions are similar ($\sigma = 0.039$ and $0.034\ \mu\text{m}^{-1}$ for Ryugu and Bennu, respectively), the distribution of color differs spatially. Ryugu shows large-scale latitudinal color differences: The latitudinal difference is ~0.5 the standard deviation of the global color variation [>99% confidence with mean difference of 0.52σ between the redder mid-latitudinal and the bluer equatorial regions (*27*)], which has been attributed to regolith migration from the equator to mid-latitudes during the spin-down of Ryugu (*68*). A latitudinal color trend is also observed on Bennu, but the difference is small compared with its overall color variation [>99% confidence with mean difference of 0.21σ (*31*)]. Bennu's slightly bluer equatorial region may indicate the presence of more mature material, which is consistent with its increasing rotation rate and the associated global patterns of mass movement across the asteroid (*43*).

Unlike Ryugu, color variation on Bennu appears to be dominated by heterogeneity at the meter scale, likely driven by boulders. This suggests that the extent of recent large-scale mass wasting on Bennu may not have been as widespread as the effect of regolith mixing. Episodes of particle ejection have been observed from Bennu's surface (*42*), redistributing its surface material over shorter time scales than those expected for mass wasting (*69*). Large-scale latitudinal spatial patterns may have been obliterated by particle ejection events, which overturn $\sim 10^4$ g of surface material per orbit (437 days) (*69*). Of the material

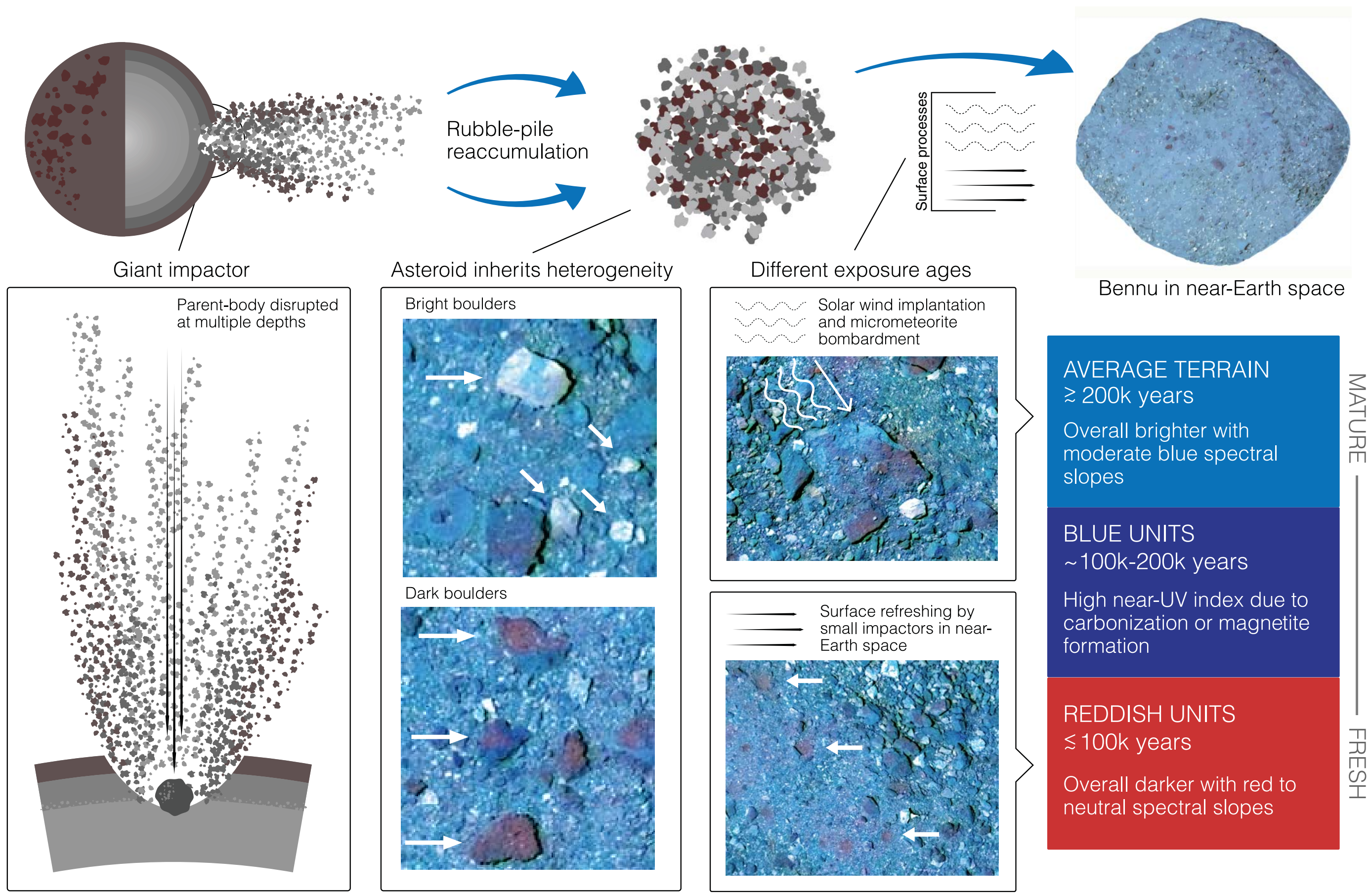

Fig. 7. Proposed model of color and reflectance diversity. We propose that distinct rock types formed at different depths on Bennu's parent body. After the parent body was catastrophically disrupted by a giant impactor, Bennu accumulated from its debris (*4*–*6*) and inherited these distinct materials, leading to the observed heterogeneity among boulders on Bennu. Since Bennu's formation and subsequent transit to near-Earth space, it has been altered by exposure to the space environment, which ultimately results in its moderately blue global color. Small near-Earth impactors also continually refresh the surface, creating craters of comparatively fresh, reddish material, which weather toward bluer colors on a time scale of $\sim 10^5$ years.

lofted, most of the mass (70 to 85%) falls back onto Bennu's surface (*69*).

Young craters on Bennu tend to be redder than the average surface, whereas their young (small) counterparts on Ryugu are bluer than average (*70*). Because Bennu's global photometric spectrum is bluer overall than Ryugu's, the absolute spectral slopes of the craters on the two asteroids are similar (fig. S14). Hayabusa2 NIR observations showed that the freshly exposed interior of the artificial SCI crater on Ryugu does not exhibit a deep hydration band at 2.7 μm (*50*), suggesting that Ryugu's dehydration is not a recent event and likely took place on the parent body (*71*). Although the colors of young craters on Ryugu and Bennu are similar, their hydration properties differ, suggesting that spectral changes in response to space weathering (e.g., bluing versus reddening) can be influenced by initial composition.

Conclusions and prospects for sample return

Bennu's surface is highly diverse, encompassing primitive material potentially from different depths in its parent body (Fig. 7). A smaller proportion consists of exogenic material from another asteroid family delivered in a predisruption impact to the parent body (*38*). Although Bennu's low average reflectance (0.044) (*4*, *10*) is dominated by the abundant dark boulders and particles formed by their breakdown, the limited latitudinal pattern in the observed heterogeneity indicates a well-mixed combination of disparate materials at spatial scales of 1 to 10 m.

Interboulder variations in reflectance and texture appear to be primordial in origin, but variations in spectral slopes among craters and between individual rock faces appear to be linked to exposure age (Fig. 7). The young age of small reddish craters and the solar orientation of intraboulder color patterns indicate that redder spectra correspond to the most recently exposed surfaces. The underlying composition of dark materials on Bennu, which potentially contain a higher proportion of organic material available for carbonization, likely leads to initial near-UV bluing of any freshly exposed redder materials. Initial bluing could also occur with the production of magnetite in response to space weathering. With age, surface materials brighten and become more neutrally sloped, consistent with Bennu's gently blue average spectral slope. This final stage of space weathering may result from accumulations of nanophase and larger metallic iron particles, which potentially have a brightening and reddening effect in low-reflectance and carbonaceous materials (*59*). It could also arise from the development of metal-like optical properties in Bennu surface materials due to progressively stronger carbonization effects, which eventually leads to brightening (*57*).

Our observations suggest that the OSIRIS-REx sample will contain materials with diverse origins and evolution even from a single location on the asteroid. Both the primary and back-up sample sites, Nightingale (56°N, 42°E) and Osprey (11.5°N, 87.5°E), are situated within small reddish craters. The redder colors and shorter 2.7-μm band minimum positions of materials in these craters imply that they are pristine, have experienced less modification from space weathering than the average Bennu surface, and potentially have a higher proportion of micrometer-scale grains.

REFERENCES AND NOTES

1. D. S. Lauretta *et al*., OSIRIS-REx: Sample return from asteroid (101955) Bennu. *Space Sci. Rev.* **212**, 925–984 (2017). doi: 10.1007/s11214-017-0405-1
2. B. E. Clark *et al*., Asteroid (101955) 1999 RQ36: Spectroscopy from 0.4 to 2.4 μm and meteorite analogs. *Icarus* **216**, 462–475 (2011). doi: 10.1016/j.icarus.2011.08.021
3. W. F. Bottke *et al*., In search of the source of asteroid (101955) Bennu: Applications of the stochastic YORP model. *Icarus* **247**, 191–217 (2015). doi: 10.1016/j.icarus.2014.09.046
4. D. N. DellaGiustina *et al*., Properties of rubble-pile asteroid (101955) Bennu from OSIRIS-REx imaging and thermal analysis. *New Astron.* **3**, 341–351 (2019). doi: 10.1038/s41550-019-0731-1
5. D. S. Lauretta *et al*., The unexpected surface of asteroid (101955) Bennu. *Nature* **568**, 55–60 (2019). doi: 10.1038/s41586-019-1033-6; pmid: 30890786
6. O. S. Barnouin *et al*., Shape of (101955) Bennu indicative of a rubble pile with internal stiffness. *Nat. Geosci.* **12**, 247–252 (2019). doi: 10.1038/s41561-019-0330-x; pmid: 31080497
7. V. E. Hamilton *et al*., Evidence for widespread hydrated minerals on asteroid (101955) Bennu. *Nat. Astron.* **3**, 332–340 (2019). doi: 10.1038/s41550-019-0722-2; pmid: 31360777
8. A. A. Simon *et al*., Widespread carbon-bearing materials on near-Earth asteroid (101955) Bennu. *Science* **370**, eabc3522 (2020). doi: 10.1126/science.abc3522
9. H. H. Kaplan *et al*., Bright carbonate veins on asteroid (101955) Bennu: Implications for aqueous alteration history. *Science* **370**, eabc3557 (2020). doi: 10.1126/science.abc3557
10. C. W. Hergenrother *et al*., The operational environment and rotational acceleration of asteroid (101955) Bennu from OSIRIS-REx observations. *Nat. Commun.* **10**, 1291 (2019). doi: 10.1038/s41467-019-09213-x; pmid: 30890725
11. A. E. Saal, E. H. Hauri, J. A. Van Orman, M. J. Rutherford, Hydrogen isotopes in lunar volcanic glasses and melt inclusions reveal a carbonaceous chondrite heritage. *Science* **340**, 1317–1320 (2013). doi: 10.1126/science.1235142; pmid: 23661641
12. C. R. Chapman, J. W. Salisbury, Comparisons of meteorite and asteroid spectral reflectivities. *Icarus* **19**, 507–522 (1973). doi: 10.1016/0019-1035(73)90078-X
13. D. Nesvorný, R. Jedicke, R. J. Whiteley, Ž. Ivezić, Evidence for asteroid space weathering from the Sloan Digital Sky Survey. *Icarus* **173**, 132–152 (2005). doi: 10.1016/j.icarus.2004.07.026
14. M. J. Gaffey *et al*., Mineralogical variations within the S-type asteroid class. *Icarus* **106**, 573–602 (1993). doi: 10.1006/icar.1993.1194
15. M. Lazzarin *et al*., Space weathering in the main asteroid belt: The big picture. *Astrophys. J.* **647**, L179–L182 (2006). doi: 10.1086/507448
16. H. M. Kaluna, J. R. Masiero, K. J. Meech, Space weathering trends among carbonaceous asteroids. *Icarus* **264**, 62–71 (2016). doi: 10.1016/j.icarus.2015.09.007
17. R. Brunetto, M. J. Loeffler, D. Nesvorný, S. Sasaki, G. Strazzulla, "Asteroid surface alteration by space weathering processes" in *Asteroids IV*, P. Michel, F. E. DeMeo, W. F. Bottke, Eds. (Univ. of Arizona Press, 2015), pp. 597–616.
18. P. Vernazza *et al*., Paucity of Tagish Lake-like parent bodies in the Asteroid Belt and among Jupiter Trojans. *Icarus* **225**, 517–525 (2013). doi: 10.1016/j.icarus.2013.04.019
19. M. Matsuoka *et al*., Pulse-laser irradiation experiments of Murchison CM2 chondrite for reproducing space weathering on C-type asteroids. *Icarus* **254**, 135–143 (2015). doi: 10.1016/j.icarus.2015.02.029
20. C. Lantz *et al*., Ion irradiation of carbonaceous chondrites: A new view of space weathering on primitive asteroids. *Icarus* **285**, 43–57 (2017). doi: 10.1016/j.icarus.2016.12.019
21. C. Lantz, R. P. Binzel, F. E. DeMeo, Space weathering trends on carbonaceous asteroids: A possible explanation for Bennu's blue slope? *Icarus* **302**, 10–17 (2018). doi: 10.1016/j.icarus.2017.11.010
22. M. S. Thompson *et al*., The effect of progressive space weathering on the organic and inorganic components of a carbonaceous chondrite. *Icarus* **346**, 113775 (2020). doi: 10.1016/j.icarus.2020.113775
23. H. M. Kaluna, H. A. Ishii, J. P. Bradley, J. J. Gillis-Davis, P. G. Lucey, Simulated space weathering of Fe-and Mg-rich aqueously altered minerals using pulsed laser irradiation. *Icarus* **292**, 245–258 (2017). doi: 10.1016/j.icarus.2016.12.028
24. M. S. Thompson, M. J. Loeffler, R. V. Morris, L. P. Keller, R. Christoffersen, Spectral and chemical effects of simulated space weathering of the Murchison CM2 carbonaceous chondrite. *Icarus* **319**, 499–511 (2019). doi: 10.1016/j.icarus.2018.09.022
25. D. N. DellaGiustina *et al*., Overcoming the challenges associated with image-based mapping of small bodies in preparation for the OSIRIS-REx mission to (101955) Bennu. *Earth Space Sci.* **5**, 929–949 (2018). doi: 10.1029/2018EA000382
26. B. Rizk *et al*., OCAMS: The OSIRIS-REx camera suite. *Space Sci. Rev.* **214**, 26 (2018). doi: 10.1007/s11214-017-0460-7
27. B. Zellner, D. J. Tholen, E. F. Tedesco, The eight-color asteroid survey: Results for 589 minor planets. *Icarus* **61**, 355–416 (1985). doi: 10.1016/0019-1035(85)90133-2
28. F. E. DeMeo, B. Carry, The taxonomic distribution of asteroids from multi-filter all-sky photometric surveys. *Icarus* **226**, 723–741 (2013). doi: 10.1016/j.icarus.2013.06.027
29. D. R. Golish *et al*., Ground and In-Flight Calibration of the OSIRIS-REx Camera Suite. *Space Sci. Rev.* **216**, 12 (2020). doi: 10.1007/s11214-019-0626-6; pmid: 32025061
30. D. R. Golish *et al*., Disk-resolved photometric modeling and properties of asteroid (101955) Bennu. *Icarus* 10.1016/j.icarus.2020.113724 (2020). doi: 10.1016/j.icarus.2020.113724
31. Materials and methods are available as supplementary materials.
32. C. A. Bennett *et al*., A high-resolution global basemap of (101955) Bennu. *Icarus* 10.1016/j.icarus.2020.113690 (2020). doi: 10.1016/j.icarus.2020.113690
33. K. J. Walsh *et al*., Craters, boulders and regolith of (101955) Bennu indicative of an old and dynamic surface. *Nat. Geosci.* **12**, 242–246 (2019). doi: 10.1038/s41561-019-0326-6
34. M. G. Daly *et al*., The OSIRIS-REx laser altimeter (OLA) investigation and instrument. *Space Sci. Rev.* **212**, 899–924 (2017). doi: 10.1007/s11214-017-0375-3
35. O. S. Barnouin *et al*., Digital terrain mapping by the OSIRIS-REx mission. *Planet. Space Sci.* **180**, 104764 (2020). doi: 10.1016/j.pss.2019.104764
36. M. G. Daly *et al*., Hemispherical differences in the shape and topography of asteroid (101955) Bennu. *Sci. Adv.* **6**, eabd3649 (2020). doi: 10.1126/sciadv.abd3649
37. D. C. Reuter *et al*., The OSIRIS-REx Visible and InfraRed Spectrometer (OVIRS): Spectral maps of the asteroid Bennu. *Space Sci. Rev.* **214**, 54 (2018). doi: 10.1007/s11214-018-0482-9
38. D. N. DellaGiustina *et al*., Exogenic Basalt on Asteroid (101955) Bennu. *New Astron.* 10.1038/s41550-020-1195-z (2020). doi: 10.1038/s41550-020-1195-z
39. J. L. Molaro *et al*., In situ evidence of thermally induced rock breakdown widespread on Bennu's surface. *Nat. Commun.* **11**, 2913 (2020). doi: 10.1038/s41467-020-16528-7; pmid: 32518333
40. C. T. Russell *et al*., Dawn at Vesta: Testing the protoplanetary paradigm. *Science* **336**, 684–686 (2012). doi: 10.1126/science.1219381; pmid: 22582253
41. F. Vilas, A cheaper, faster, better way to detect water of hydration on Solar System bodies. *Icarus* **111**, 456–467 (1994). doi: 10.1006/icar.1994.1156
42. D. S. Lauretta *et al*., Episodes of particle ejection from the surface of the active asteroid (101955) Bennu. *Science* **366**, eaay3544 (2019). doi: 10.1126/science.aay3544; pmid: 31806784
43. E. R. Jawin *et al*., Global patterns of mass movement on asteroid (101955) Bennu. *J. Geophys. Res. Planets* **125**, e2020JE006475 (2020). doi: 10.1029/2020JE006475
44. A. R. Hendrix, F. Vilas, C-complex asteroids: UV-visible spectral characteristics and implications for space weathering effects. *Geophys. Res. Lett.* **46**, 14307–14317 (2019). doi: 10.1029/2019GL085883
45. W. F. Bottke Jr. *et al*., Linking the collisional history of the main asteroid belt to its dynamical excitation and depletion. *Icarus* **179**, 63–94 (2005). doi: 10.1016/j.icarus.2005.05.017

46. S. Marchi *et al*., The cratering history of asteroid (2867) Steins. *Planet. Space Sci.* **58**, 1116–1123 (2010). doi: 10.1016/j.pss.2010.03.017
47. P. Brown, R. E. Spalding, D. O. ReVelle, E. Tagliaferri, S. P. Worden, The flux of small near-Earth objects colliding with the Earth. *Nature* **420**, 294–296 (2002). doi: 10.1038/nature01238; pmid: 12447433
48. A. W. Harris, G. D'Abramo, The population of near-Earth asteroids. *Icarus* **257**, 302–312 (2015). doi: 10.1016/j.icarus.2015.05.004
49. S. Marchi, C. R. Chapman, O. S. Barnouin, J. E. Richardson, J.-B. Vincent, "Cratering on asteroids" in *Asteroids IV*, P. Michel, F. E. DeMeo, W. F. Bottke, Eds. (Univ. of Arizona Press, 2015), pp. 725–744.
50. M. Arakawa *et al*., An artificial impact on the asteroid (162173) Ryugu formed a crater in the gravity-dominated regime. *Science* **368**, 67–71 (2020). doi: 10.1126/science.aaz1701; pmid: 32193363
51. E. Tatsumi, S. Sugita, Cratering efficiency on coarse-grain targets: Implications for the dynamical evolution of asteroid 25143 Itokawa. *Icarus* **300**, 227–248 (2018). doi: 10.1016/j.icarus.2017.09.004
52. L. P. Keller, E. L. Berger, A transmission electron microscope study of Itokawa regolith grains. *Earth Planets Space* **66**, 71 (2014). doi: 10.1186/1880-5981-66-71
53. T. V. Johnson, F. P. Fanale, Optical properties of carbonaceous chondrites and their relationship to asteroids. *J. Geophys. Res.* **78**, 8507–8518 (1973). doi: 10.1029/JB078i035p08507
54. C. M. Hartzell, Dynamics of 2D electrostatic dust levitation at asteroids. *Icarus* **333**, 234–242 (2019). doi: 10.1016/j.icarus.2019.05.013
55. M. C. Nolan *et al*., Detection of rotational acceleration of Bennu using HST light curve observations. *Geophys. Res. Lett.* **46**, 1956–1962 (2019). doi: 10.1029/2018GL080658
56. W. F. Bottke *et al*., Meteoroid Impacts as a Source of Bennu's Particle Ejection Events. *J. Geophys. Res. Planets* **125**, e2019JE006282 (2020). doi: 10.1029/2019JE006282
57. L. Moroz *et al*., Optical alteration of complex organics induced by ion irradiation: 1. Laboratory experiments suggest unusual space weathering trend. *Icarus* **170**, 214–228 (2004). doi: 10.1016/j.icarus.2004.02.003
58. B. Hapke, Space weathering from Mercury to the asteroid belt. *J. Geophys. Res. Planets* **106**, 10039–10073 (2001). doi: 10.1029/2000JE001338
59. A. S. Rivkin, E. S. Howell, F. Vilas, L. A. Lebofsky, "Hydrated minerals on asteroids: The astronomical record" in *Asteroids III*, W. F. Bottke, A. Cellino, P. Paolicchi, R. P. Binzel (Univ. of Arizona Press, 2002), pp. 235–253.
60. B. Rozitis *et al*., Asteroid (101955) Bennu's weak boulders and thermally anomalous equator. *Sci. Adv.* **6**, eabc3699 (2020). doi: 10.1126/sciadv.abc3699
61. C. A. Johnson, M. Prinz, Carbonate compositions in CM and CI chondrites and implications for aqueous alteration. *Geochim. Cosmochim. Acta* **57**, 2843–2852 (1993). doi: 10.1016/0016-7037(93)90393-B
62. A. Morlok *et al*., Brecciation and chemical heterogeneities of CI chondrites. *Geochim. Cosmochim. Acta* **70**, 5371–5394 (2006). doi: 10.1016/j.gca.2006.08.007
63. J. Alfing, M. Patzek, A. Bischoff, Modal abundances of coarse-grained (> 5 μm) components within CI-chondrites and their individual clasts–Mixing of various lithologies on the CI parent body(ies). *Geochemistry* **79**, 125532 (2019). doi: 10.1016/j.chemer.2019.08.004
64. E. A. Cloutis *et al*., Spectral reflectance properties of HED meteorites CM2 carbonaceous chondrites: Comparison to HED grain size and compositional variations and implications for the nature of low-albedo features on Asteroid 4 Vesta. *Icarus* **223**, 850–877 (2013). doi: 10.1016/j.icarus.2013.02.003
65. M. R. Izawa *et al*., Spectral reflectance properties of magnetites: Implications for remote sensing. *Icarus* **319**, 525–539 (2019). doi: 10.1016/j.icarus.2018.10.002
66. C. M. Alexander, R. Bowden, M. L. Fogel, K. T. Howard, Carbonate abundances and isotopic compositions in chondrites. *Meteorit. Planet. Sci.* **50**, 810–833 (2015). doi: 10.1111/maps.12410
67. J. de León *et al*., Expected spectral characteristics of (101955) Bennu and (162173) Ryugu, targets of the OSIRIS-REx and Hayabusa2 missions. *Icarus* **313**, 25–37 (2018). doi: 10.1016/j.icarus.2018.05.009
68. S. Sugita *et al*., The geomorphology, color, and thermal properties of Ryugu: Implications for parent-body processes. *Science* **364**, 252 (2019). doi: 10.1126/science.aaw0422; pmid: 30890587
69. C. W. Hergenrother *et al*., Photometry of particles ejected from active asteroid (101955) Bennu. *J. Geophys. Res. Planets* **125**, e2020JE006381 (2020). doi: 10.1029/2020JE006381
70. T. Morota *et al*., Sample collection from asteroid (162173) Ryugu by Hayabusa2: Implications for surface evolution. *Science* **368**, 654–659 (2020). doi: 10.1126/science.aaz6306; pmid: 32381723
71. K. Kitazato *et al*., "Asteroid 162173 Ryugu: Surface composition as observed by Hayabusa2/NIRS3," in *EPSC Abstracts*, vol. 13, EPSC-DPS2019-1376-1 (EPSC, 2019); https://meetingorganizer.copernicus.org/EPSC-DPS2019/EPSC-DPS2019-1376-1.pdf.
72. D. DellaGiustina, Maps_DellaGiustina_et_al_Science_2020_abc3660, Version 2, figshare (2020); https://doi.org/10.6084/m9.figshare.12996494.

ACKNOWLEDGMENTS

We thank the entire OSIRIS-REx Team for making the encounter with Bennu possible. For fig. S5, we thank D. Rachford and IMV Minerals for providing the SAP105 sample and S. Mertzman of Franklin and Marshall College for confirming the composition of the SAP105 sample. We thank R. J. Burmeister for assistance with graphic design of the figures. **Funding:** D.N.D., K.N.B., K.J.W., P.H.S., D.R.G., E.B.B., R.L.B., T.B., H.C., B.E.C., A.S., K.B., C.A.B., W.F.B., J.I.B., H.C.C., C.Y.D.D., K.L.E., V.E.H., C.W.H., E.S.H., E.R.J., H.H.K., L.L.C., L.L., J.Y.L., M.C.N., J.N., N.A.P., B.Ri., A.J.R., N.K.S., A.A.S., C.W.V.W., and D.S.L. were supported by NASA under contract NNM10AA11C issued through the New Frontiers Program. J.L.M. and D.T. were supported by the NASA OSIRIS-REx Participating Scientist Program 80NSSC18K0230. A.R.H. was supported by the NASA Solar System Exploration Research Virtual Institute 2016 (SSERVI16) Cooperative Agreement TREX NNH16ZDA001N. E.T., K.Y., and S.S. were supported by the Japanese Society for Promotion of Science (JSPS) Core-to-Core program "International Planetary Network." The OLA instrument and funding for M.G.D. and M.M.A.A. and support for A.P., E.A.C., and D.M.A., were provided by the Canadian Space Agency. J.L.R., E.T., M.Po., and J.d.L. acknowledge support from the project AYA2017-89090-P of the Spanish MINECO and from the project ProID2017010112 under the OP-ERDF-ESF and the Canarian Agency for Research, Innovation and Information Society (ACIISI). M.Pa. was supported by the Italian Space Agency (ASI) under the ASI-INAF agreement no. 2017-37-H.0. C.A., J.D.P.D., M.A.B., M.D., P.H.H., P.M., and S.F. acknowledge support from the French space agency CNES. P.M. also acknowledges support from the European Union's Horizon 2020 research and innovation program under grant agreement no. 870377 (project NEO-MAPP). C.A. was also supported by the French National Research Agency under the project "Investissements d'Avenir" UCAJEDI (ANR-15-IDEX-01). C.A. and M.D. also acknowledge support from the ANR "ORIGINS" (ANR-18-CE31-0014). B.Ro. acknowledges support from the Royal Astronomical Society (RAS) and the UK Science and Technology Facilities Council (STFC). **Author contributions:** D.N.D., P.H.S., D.R.G., B.Ri., and C.Y.D.D. planned and calibrated OCAMS MapCam and PolyCam observations of Bennu. D.N.D., K.N.B., P.H.S., D.R.G., T.L.B., K.J.B., C.A.B., J.I.B., K.L.E., L.L.C., and N.K.S. created MapCam color parameter maps of Bennu. K.N.B., E.B.B., J.N., D.T., and R.B.V.A. mapped craters and boulders on Bennu. D.N.D., K.N.B., K.J.W., P.H.S., E.B.B., R.-L.B., M.M.A.A., and W.F.B. performed the statistical analysis of boulder and craters colors. E.T., K.Y., and S.S. performed comparisons of the colors of Bennu and Ryugu. E.A.C., B.E.C., A.R.H., A.S., D.M.A., and A.P. performed comparisons between Bennu colors and laboratory spectra. J.D.P.D., A.A.S., H.H.K., and V.E.H. processed and interpreted OVIRS observations of Bennu. M.G.D., M.M.A.A., R.-L.B., and N.A.P. processed and interpreted OLA observations of Bennu. D.N.D., P.H.S., D.R.G., K.J.W., R.-L.B., H.C., C.A., M.A.B., H.C.C.Jr., M.D., J.d.L., S.F., V.E.H., P.H.H., C.W.H., E.S.H., E.R.J., H.H.K., L.F.L., J.Y.L., P.M., J.L.M., M.C.N., M.Pa., M.Po., A.J.R., B.Ro., A.A.S., D.T., and C.W.V.W. contributed to the conceptualization and writing. D.S.L. contributed to the conceptualization and leads the OSIRIS-REx mission. **Competing interests:** We declare no competing interests. **Data and materials availability:** Full-resolution MapCam color maps of Bennu, as shown in Fig. 1 and fig. S5, are available at figshare (*72*). Catalogs of the boulders and craters we used are available as data S1 and S2, respectively. The stereophotoclinometry v28 and OLA v20 shape models of Bennu are available through the Small Body Mapping Tool at http://sbmt.jhuapl.edu/. Detailed Survey OCAMS (MapCam and PolyCam), Orbital B OLA, and Detailed Survey and Recon A OVIRS data are available via the Planetary Data System (PDS) at: https://sbnarchive.psi.edu/pds4/orex/orex.ocams/data_calibrated/detailed_survey/, https://sbnarchive.psi.edu/pds4/orex/orex.ocams/data_calibrated/recon/, https://sbnarchive.psi.edu/pds4/orex/orex.ola/data_calibrated/orbit_b/, https://sbnarchive.psi.edu/pds4/orex/orex.ovirs/data_calibrated/detailed_survey/, and https://sbnarchive.psi.edu/pds4/orex/certified/orex.ovirs/data_calibrated/recon/, respectively. The list of MapCam images used to produce the maps in Fig. 1 is available as data S3.

SUPPLEMENTARY MATERIALS

science.sciencemag.org/content/370/6517/eabc3660/suppl/DC1
Materials and Methods
Figs. S1 to S16
Tables S1 and S2
References (*73*–*91*)
Data S1 to S3

21 April 2020; accepted 24 September 2020
Published online 8 October 2020
10.1126/science.abc3660

Science

Variations in color and reflectance on the surface of asteroid (101955) Bennu

D. N. DellaGiustina, K. N. Burke, K. J. Walsh, P. H. Smith, D. R. Golish, E. B. Bierhaus, R.-L. Ballouz, T. L. Becker, H. Campins, E. Tatsumi, K. Yumoto, S. Sugita, J. D. Prasanna Deshapriya, E. A. Cloutis, B. E. Clark, A. R. Hendrix, A. Sen, M. M. Al Asad, M. G. Daly, D. M. Applin, C. Avdellidou, M. A. Barucci, K. J. Becker, C. A. Bennett, W. F. Bottke, J. I. Brodbeck, H. C. Connolly Jr., M. Delbo, J. de Leon, C. Y. Drouet d'Aubigny, K. L. Edmundson, S. Fornasier, V. E. Hamilton, P. H. Hasselmann, C. W. Hergenrother, E. S. Howell, E. R. Jawin, H. H. Kaplan, L. Le Corre, L. F. Lim, J. Y. Li, P. Michel, J. L. Molaro, M. C. Nolan, J. Nolau, M. Pajola, A. Parkinson, M. Popescu, N. A. Porter, B. Rizk, J. L. Rizos, A. J. Ryan, B. Rozitis, N. K. Shultz, A. A. Simon, D. Trang, R. B. Van Auken, C. W. V. Wolner and D. S. Lauretta

Science **370** (6517), eabc3660.
DOI: 10.1126/science.abc3660originally published online October 8, 2020

The complex history of Bennu's surface

The near-Earth asteroid (101955) Bennu is a carbon-rich body with a rubble pile structure, formed from debris ejected by an impact on a larger parent asteroid. The Origins, Spectral Interpretation, Resource Identification, Security, Regolith Explorer (OSIRIS-REx) spacecraft is designed to collect a sample of Bennu's surface and return it to Earth. After arriving at Bennu, OSIRIS-REx performed a detailed survey of the asteroid and reconnaissance of potential sites for sample collection. Three papers present results from those mission phases. DellaGiustina *et al.* mapped the optical color and albedo of Bennu's surface and established how they relate to boulders and impact craters, finding complex evolution caused by space weathering processes. Simon *et al.* analyzed near-infrared spectra, finding evidence for organic and carbonate materials that are widely distributed across the surface but are most concentrated on individual boulders. Kaplan *et al.* examined more detailed data collected on the primary sample site, called Nightingale. They identified bright veins with a distinct infrared spectrum in some boulders, which they interpreted as being carbonates formed by aqueous alteration on the parent asteroid. Together, these results constrain Bennu's evolution and provide context for the sample collected in October 2020.

Science, this issue p. eabc3660, p. eabc3522, p. eabc3557

Science (print ISSN 0036-8075; online ISSN 1095-9203) is published by the American Association for the Advancement of Science, 1200 New York Avenue NW, Washington, DC 20005. The title *Science* is a registered trademark of AAAS.

Science (print ISSN 0036-8075; online ISSN 1095-9203) is published by the American Association for the Advancement of Science, 1200 New York Avenue NW, Washington, DC 20005. The title *Science* is a registered trademark of AAAS.